Electrocatalysis

Deutsche Ausgabe: DOI: 10.1002/ange.201509616
Internationale Ausgabe: DOI: 10.1002/anie.201509616

Single-Crystalline Ultrathin Nickel Nanosheets Array from In Situ Topotactic Reduction for Active and Stable Electrocatalysis

*Yun Kuang[+], Guang Feng[+], Pengsong Li, Yongmin Bi, Yaping Li, and Xiaoming Sun**

Abstract: *Simultaneously synthesizing and structuring atomically thick or ultrathin 2D non-precious metal nanocrystal may offer a new class of materials to replace the state-of-art noble-metal electrocatalysts; however, the synthetic strategy is the bottleneck which should be urgently solved. Here we report the synthesis of an ultrathin nickel nanosheet array (Ni-NSA) through in situ topotactic reduction from $Ni(OH)_2$ array precursors. The Ni nanosheets showed a single-crystalline lamellar structure with only ten atomic layers in thickness and an exposed (111) facet. Combined with a superaerophobic (low bubble adhesive) arrayed structure the Ni-NSAs exhibited a dramatic enhancement on both activity and stability towards the hydrazine-oxidation reaction (HzOR) relative to platinum. Furthermore, the partial oxidization of Ni-NSAs in ambient atmosphere resulted in effective water-splitting electrocatalysts for the hydrogen-evolution reaction (HER).*

Two-dimensional (2D) crystals with atomic thickness have attracted extensive attention because of the dramatically increased surface/volume ratio and unique electronic structures.[1–9] Thus, they have been considered as promising materials in electronics,[10–14] optics,[15,16] magnetics,[17,18] and catalysis.[19,20]

Active and stable metal-based 2D crystals have shown a great potential as efficient electrocatalysts.[6,21] However, the bottom-up synthesis of ultrathin nanosheets mainly relies on whether the material itself has a lamellar structure,[3,21–24] while metal atoms have a strong preference for close-packed crystalline structures,[25–29] and rich dangling bonds would make the nanosheets extremely active and unstable.[30] Therefore, ultrathin metallic 2D structures with a plethora of unsaturated atoms are difficult to stabilize and only quite a few ligand-capped noble-metal ultrathin structures can be synthesized.[6,30–32] Up to now, non-ligand-caped 2D transition-metal nanostructures remained big synthetic challenges.

On the other hand, liquid exfoliation of organic–inorganic precursors has been demonstrated an effective way for preparation of atomically thick 2D crystals with a non-layered structure as well as the quasi-layered structure, but this strategy is so far not applicable to 2D metallic nanostructures.[33,34] Therefore, developing a new synthetic route for ultrathin 2D metallic nanostructures, especially non-noble metals, will greatly expand the 2D material family and promote their applications.

Here, we synthesized ultrathin nickel nanosheets by gently reducing a $Ni(OH)_2$ nanosheet array on a metal substrate under mild reducing conditions. The slow conversion kinetics kept the ultrathin nanosheet morphology and atomic thickness. The Ni nanosheets showed a single-crystalline lamellar structure with a thickness of only ten atomic layers and an exposed (111) facet. With plenty of active surface atoms, a single-crystalline structure, a superaerophobic (low bubble adhesive) surface, and a tunable surface state, the Ni-NSA showed a dramatic enhancement of both activity and stability on the hydrazine-oxidation reaction (HzOR) and hydrogen-evolution reaction (HER) relative to platinum, demonstrating the promising electrocatalytic applications of such ultrathin non-precious metal nanosheets.

Scheme 1 shows the in situ topotactic reduction procedure of the ultrathin Ni-NSA. Firstly, $Ni(OH)_2$ nanowall arrays were grown on a nickel foam following our previous report,[35] as evidenced by the X-ray diffraction (XRD) pattern (Figure 1 A) of typical $Ni(OH)_2$ peaks after growth of $Ni(OH)_2$ arrays on a Ni substrate. Then the as-formed $Ni(OH)_2$ nanowalls were solvothermally reduced in ethylene glycol

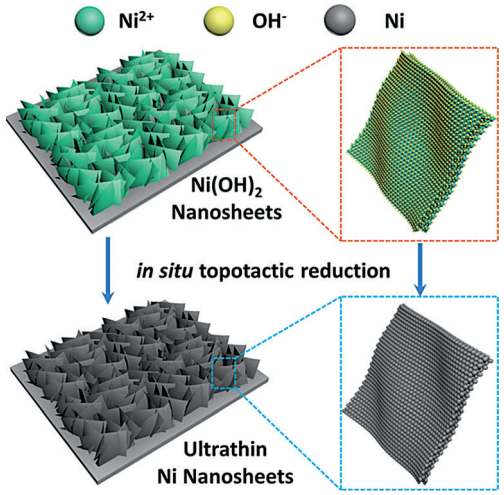

Scheme 1. In situ topotactic reduction method for fabrication of the atomically layered Ni nanosheet array.

[*] Dr. Y. Kuang,[+] G. Feng,[+] P. Li, Y. Bi, Dr. Y. Li, Prof. X. Sun
State Key Laboratory of Chemical Resource Engineering
Beijing University of Chemical Technology
Beijing 100029 (P.R. China)
E-mail: sunxm@mail.buct.edu.cn

[+] These authors contributed equally to this work.

Supporting information and ORCID(s) from the author(s) for this article are available on the WWW under http://dx.doi.org/10.1002/anie.201509616.

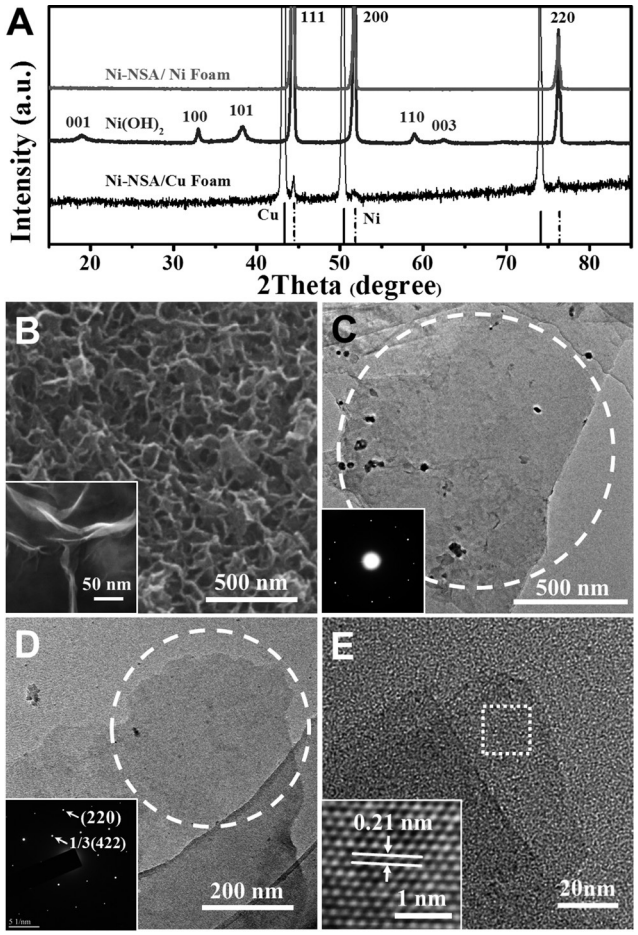

Figure 1. A) XRD pattern of the $Ni(OH)_2$ nanosheet array and Ni-NSA grown on an Ni foam substrate and a Cu foam substrate. The two lines at the base show standard XRD patterns of Cu and Ni metals. B) SEM and HRSEM (inset) images of as synthesized Ni-NSA. C,D) TEM and corresponding electron diffraction pattern of C) two overlapped Ni nanosheets and D) a single layered region, demonstrating a single-crystalline structure. E) HRTEM image (inset shows crystal lattices) of Ni nanosheets.

assisted by NaOH.[36] The exclusive face-centered cubic (fcc) phase Ni patterns of the sample after reduction suggested complete reduction from $Ni(OH)_2$ to Ni. In order to confirm that the reduced product was Ni and to exclude the influence of the Ni substrate, the same Ni-NSA sample was synthesized on a Cu substrate (black line in Figure 1 A, see Figure S1 in the Supporting Information for a SEM image). Appearance of (111), (200), and (220) peaks of the Ni crystal confirmed complete reduction of the sample.

The morphology of the obtained ultrathin Ni-NSA was characterized by scanning electron microscopy (SEM) and transmission electron microscopy (TEM). Figure 1 B shows a 3D open porous array structure of the reduced Ni nanosheets, and each nanosheet was vertically grown on the substrate with hundreds of nanometers in size. However, the thickness of the nanosheets was as thin as only several nanometers, which could be read from the HRSEM image. The relatively low contrast of the nanosheets in the TEM images (Figure 1 C–E) implied ultrathin structures. The electron diffraction pattern of the two overlapping Ni nanosheets (Figure 1 C inset, S2) revealed the single crystallinity of the as-obtained Ni nanosheets while the electron diffraction pattern (Figure 1 D) and enlarged HRTEM image (Figure 1 E inset) of a single-layered region show face-centered cubic (fcc) nickel with 1/3(422) and (220) lattices on the sheet plane, which is in good agreement with previous observations on metallic fcc nanoplatelets,[6] suggesting the nickel nanosheets have (111) basal planes.

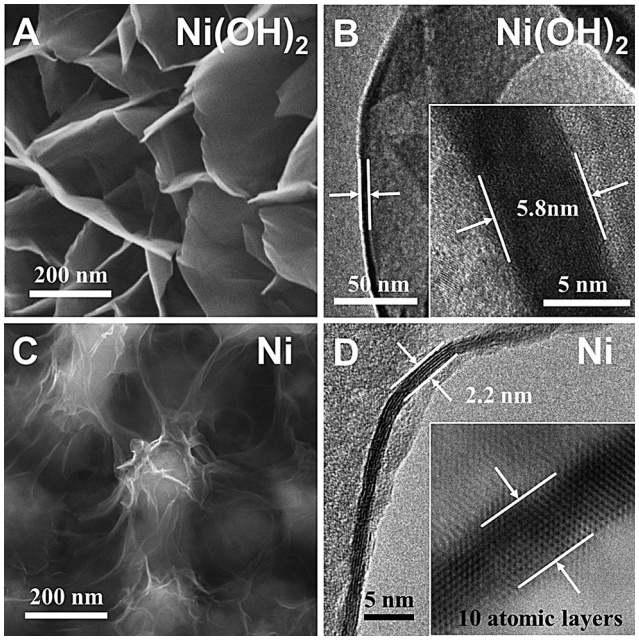

Figure 2. A,C) SEM images of an as-synthesized $Ni(OH)_2$ nanowall array and Ni-NSA. B,D) HRTEM image of a scrolled $Ni(OH)_2$ nanowall and a vertically laid Ni nanosheet. The inset shows the thickness of the $Ni(OH)_2$ nanowall and Ni nanosheet.

Figure 2 reveals the morphology inherence between Ni-NSA and the $Ni(OH)_2$ nanowall array (i.e. in situ conversion). SEM images (Figure 2 A and C) show that Ni-NSA inherit the high porosity of the $Ni(OH)_2$ array after in situ conversion, but the Ni nanosheets were much thinner than the $Ni(OH)_2$ nanowalls. The HRTEM image of a scrolled $Ni(OH)_2$ nanowall (Figure 2 B) shows that the thickness of the nanowall was in the range of 5–6 nm (i.e. 10–12 Ni layers), while the Ni nanosheet (Figure 2 D) was as thin as only 2.2 nm (i.e. 10 atomic layers) typically, demonstrating an ultrathin lamellar structure. The coincidence of the Ni atomic layer numbers suggests an in situ topotactic reduction pathway from the $Ni(OH)_2$ nanowall array to Ni-NSA. Characterization and analysis on the topotactic conversion intermediates (0, 3 , 6, 9, and 12 h) through HRTEM, electron diffraction patterns (Figure S3), and XRD patterns (Figure S4) revealed that the in situ reduction from $Ni(OH)_2$ to Ni experienced a phase transformation from hexagonal phased $Ni(OH)_2$ to cubic phased NiO through dehydration, followed by a reduction from cubic NiO to fcc Ni.

A lamellar structure is not thermodynamically favorable for fcc metallic structures; therefore, the in situ reduction

kinetics must be well-controlled to avoid self-nucleation. Lower temperatures (< 140 °C) would resulted in incomplete reduction of $Ni(OH)_2$ (Figure S5B–C) while higher temperatures (> 180 °C) would lead to a too fast reduction and cause new nucleation, resulting in nanospheres (Figure S5E-F).

The single-crystalline ultrathin 2D structure endowed Ni-NSA with an extremely high ratio of surface atoms and structure stability (low atom mobility), which was demonstrated by ultrahigh electrocatalytic performance (Figure 3).

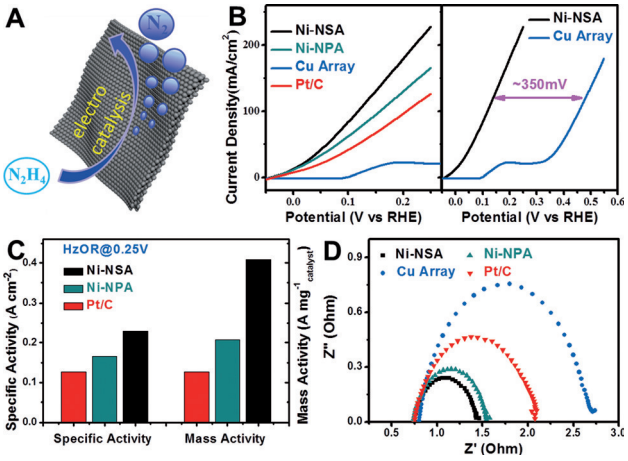

Figure 3. A) Schematic of the Ni-NSA catalytic hydrazine oxidation. B) HzOR performance of Ni-NSA, 3D porous Ni nanoparticle assembly (Ni-NPA), Cu nanosheet array, and commercial Pt/C (loaded on a Ni foam). C) Comparison of the specific activity and mass activity of Ni-NSA, Ni-NPAs, and 20 wt% Pt/C. An 81% enhancement was observed for Ni-NSA. The specific activity and mass activity were currents normalized to geometric areas of the nickel foam substrates and the mass loading of the samples, respectively. D) Nyquist plots of the four electrodes, indicating that Ni-NSA possessed a much smaller charge-transfer resistance. Note: the loading amount of Pt/C was twice that of Ni-NSA because of the poor adhesion to the substrate. The mass loadings of Ni-NSA and Ni-NPA were 0.59 mg cm^{-2} and 0.81 mg cm^{-2}, respectively.

As an example, Figure 3B compares the electrocatalytic hydrazine oxidation (HzOR) performance of Ni-NSA, 3D porous Ni nanoparticle assembly (Ni-NPA), commercial Pt/C (loaded on Ni foam), and reported Cu nanosheet array[37] electrodes. The onset potential (E_{on}) of Ni-NSA was about 300 mV lower than that reported for the Cu nanosheet array and even lower than that of Pt/C, demonstrating a much higher intrisic activity. For quantitative comparison, the kinetic currents were normalized to the active area of the substrates and the mass loading of the catalysts (Figure 3C), respectively. At the same potential of 0.25 V, the Ni-NSA electrode afforded a considerable specific activity (227.6 mA cm^{-2}) and mass activity (406.4 mA mg$^{-1}_{catalyst}$), which were 1.81 times and 3.25 times higher than that of the Pt/C catalyst. Besides the high intrinsic activity, the ultrathin Ni-NSAs also possess rough surfaces, which could cut the liquid–solid–gas three-phase contact line into tiny pieces during the electrocatalytic gas-evolution process, thus exhibiting superaerophobic surfaces, like the MoS_2 nanosheet arrays previously reported by us.[38] Such superaerophobic surfaces could facilitate mass transfer on catalyst surfaces and thus facilitate a current increase during electrocatalysis. As shown in adhesion force tests in Figure S6, the Ni-NSAs showed almost no adhesion force to the gas bubbles; in contrast to the severe adhesion force of Pt/C. Thus, the superaerophobic Ni-NSA showed a small releasing size and fast removal of as-formed N_2 gas bubbles (Movie S1) while severe adhesion of gas bubbles on the Pt/C-Ni foam led to serious blockage of the electrocatalytic active sites, resulting in a much bigger releasing size of the bubbles and a low electrocatalytic performance (Movie S2). No cleaning/activation step was involved for Ni-NSA before the HzOR test, implying clean surfaces of the products.

In order to further illustrate the advances of atomically thick 2D structure, we prepared a 3D porous Ni nanoparticle assembly sample for comparison (Ni-NPA, see the SEM image in Figure S7 for the morphology) following a similar procedure but under harsher reduction conditions. The Ni-NPA was deliberately made 3D open porous and superaerophobic, thus both Ni-NSA and Ni-NPA were composed of the same materials and showed similar surface properties. A comparison of their electrocatalytic performances reflected the intrinsic property difference. As shown in Figure 3, Ni-NSA exhibited a 1.97 times higher activity (Figure 3C) and a lower charge-transfer resistance (ca. 69 Ω) in Nyquist plots (Figure 3D), revealing a much higher intrinsic electrocatalytic performance, largely because of its ultrathin 2D structure, ultrahigh surface area, and a plethora of unsaturated atoms (i.e. surface atoms, step/corner atoms), which could act as highly active electrocatalytic sites.[39] Combined with a single-crystalline structure and superaerophobic surfaces, the Ni-NSA showed 91.8% (Figure S8) of its original current density and no structural damage (Figure S9) after a 10000 s harsh stability test in highly concentrated N_2H_4 solution, suggesting long-term stability.

The Ni-NSAs also showed a high activity towards the hydrogen-evolution reaction (HER) after partial oxidation by exposure in ambient atmosphere for a while (Figure 4A,C). The HRTEM image (Figure 4B) and the corresponding fast Fourier transformation (FFT) pattern of a partially oxidized Ni nanosheet show two crystalline lattices that are indexed as Ni 1/3(422) and NiO 1/3(422) facets, revealing the existence of NiO on Ni surfaces. However, the NiO signal in the FFT pattern was relatively weak, demonstrating that only a small part of the surfaces was oxidized. X-ray photoelectron spectroscopy (XPS) spectroscopy confirmed the co-existence of Ni^{II} and Ni^0 (Figure S10).

Surprisingly, it is found that partial oxidization of Ni-NSAs under low-pressure air conditions (vacuum oven, ca. 1×10^3 Par) for 6 h showed the best HER performance (Figure 4C). Under this condition, the Ni/NiO-NSAs showed an onset potential of −34 mV in 0.1 M KOH (Figure 4D inset) and a Tafel slope of 114 mV per decade (Figure S11), which is better than that of the Ni/NiO-NPA counterpart (135 mV per decade) because of its structural advantage. Besides, the current increase of Ni/NiO-NSAs was much faster than that of Pt/C at a higher current (e.g. 100 mA cm^{-2}, Figure 4D) because of its high surface area and superaerophobic surface structure. The ultrathin Ni/NiO-NSA also exhibited a very

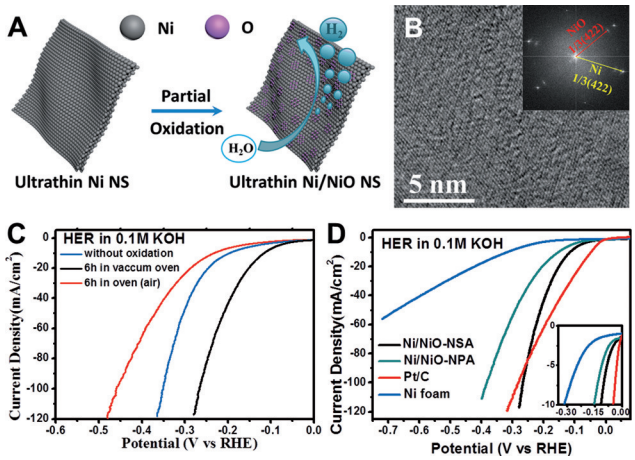

Figure 4. A) Schematic of partial oxidization on the Ni-NSA surface. B) HRTEM image and corresponding fast Fourier transformation (FFT) of a Ni nanosheet exposed in ambient atomsphere. C) HER performance of Ni/NiO-NSAs with different oxidation degree. D) HER polarization curves of Ni/NiO-NSAs, 3D porous Ni/NiO nanoparticle assembly (Ni/NiO-NPA), pure Ni foam, and commercial Pt/C (loaded on the Ni foam). Note: the loading amount of Pt/C was twice that of Ni/NiO-NSA because of the poor adhesion to the substrate.

high electrocatalytic stability. After 10 h stability testing, the Ni/NiO-NSAs still showed 94.9% (Figure S12) of its initial current density and no structural damage was found (Figure S9).

Such high HER performance was ascribed to a synergistic HER catalytic activity on the Ni/NiO interface reported by Dai and co-workers.[40] The OH^- generated by H_2O splitting preferred to attach to a NiO site at the interface because of a strong electrostatic affinity to the locally positively charged Ni^{2+} species and more unfilled d orbitals in Ni^{2+} than Ni metal, while a nearby Ni site would facilitate hydrogen adsorption and thus the Volmer process. Theoretical calculation revealed that desorption of H_2 on Ni/NiO (111) surfaces possesses a lower energy barrier (3.228 eV) than on pure Ni (111) surfaces (3.763 eV), supporting the above hypothesis.

In summary, ultrathin nickel nanosheet arrays (Ni-NSAs) were synthesized through a well-controlled in situ topotactic reduction/conversion kinetical process. Such method could achieve ultrathin nanostructures while maintain the original 2D morphology of the precursors. With plenty of active surface atoms and single-crystalline structure, the as-prepared ultrathin Ni-NSA was demonstrated as highly effective electrocatalysts for fuel-cell and water-splitting application with activity and stability higher than that of Pt. The in situ conversion method opened up a way for fabrication of 2D non-precious metal nanostructures and should be beneficial to the preparation of low-cost, highly efficient, and stable electrocatalysts and other related nanomaterials.

Experimental Section

$Ni(OH)_2$ nanowall films were synthesized following our previous report.[35] In a typical in situ topotactic reduction procedure, NaOH (1 g) and ethylene glycol (EG; 36 mL) were put into a 40 mL Teflon-lined stainless-steel autoclave, and stirred until the solid dissolved. Then $Ni(OH)_2$ nanowall films were transferred to the autoclave and maintained at 160 °C for 12 h to yield the final products. The thin nanosheets on the metal substrate were rinsed several times with distilled water and ethanol (all the solvents were bubbled with Ar to eliminate solved oxygen). The Ni-NSA should be stored in an environment without oxygen to avoid oxidation.

Acknowledgements

This work was supported by National Natural Science Foundation of China, the 973 Program (grant numbers 2011CBA00503 and 2011CB932403), and the Program for Changjiang Scholars and Innovative Research Team in the University.

Keywords: electrocatalysis · nanosheets · nickel · single crystals · ultrathin films

How to cite: *Angew. Chem. Int. Ed.* **2016**, *55*, 693–697
Angew. Chem. **2016**, *128*, 703–707

[1] A. K. Geim, K. S. Novoselov, *Nat. Mater.* **2007**, *6*, 183–191.
[2] M. Chhowalla, H. S. Shin, G. Eda, L.-J. Li, K. P. Loh, H. Zhang, *Nat. Chem.* **2013**, *5*, 263–275.
[3] K. S. Novoselov, D. Jiang, F. Schedin, T. J. Booth, V. V. Khotkevich, S. V. Morozov, A. K. Geim, *Proc. Natl. Acad. Sci. USA* **2005**, *102*, 10451–10453.
[4] B. Radisavljevic, A. Radenovic, J. Brivio, V. Giacometti, A. Kis, *Nat. Nanotechnol.* **2011**, *6*, 147–150.
[5] S. Z. Butler, S. M. Hollen, L. Cao, Y. Cui, J. A. Gupta, H. R. Gutiérrez, T. F. Heinz, S. S. Hong, J. Huang, A. F. Ismach, E. Johnston-Halperin, M. Kuno, V. V. Plashnitsa, R. D. Robinson, R. S. Ruoff, S. Salahuddin, J. Shan, L. Shi, M. G. Spencer, M. Terrones, W. Windl, J. E. Goldberger, *ACS Nano* **2013**, *7*, 2898–2926.
[6] X. Huang, S. Tang, X. Mu, Y. Dai, G. Chen, Z. Zhou, F. Ruan, Z. Yang, N. Zheng, *Nat. Nanotechnol.* **2011**, *6*, 28–32.
[7] Y. Sun, Z. Sun, S. Gao, H. Cheng, Q. Liu, J. Piao, T. Yao, C. Wu, S. Hu, S. Wei, Y. Xie, *Nat. Commun.* **2012**, *3*, 1057.
[8] Y. Sun, S. Gao, F. Lei, Y. Xie, *Chem. Soc. Rev.* **2015**, *44*, 623–636.
[9] M. Xu, T. Liang, M. Shi, H. Chen, *Chem. Rev.* **2013**, *113*, 3766–3798.
[10] K. S. Novoselov, A. K. Geim, S. V. Morozov, D. Jiang, Y. Zhang, S. V. Dubonos, I. V. Grigorieva, A. A. Firsov, *Science* **2004**, *306*, 666–669.
[11] M. Osada, T. Sasaki, *Adv. Mater.* **2012**, *24*, 210–228.
[12] Y. Zhang, Y.-W. Tan, H. L. Stormer, P. Kim, *Nature* **2005**, *438*, 201–204.
[13] A. Pronschinske, P. Pedevilla, C. J. Murphy, E. A. Lewis, F. R. Lucci, G. Brown, G. Pappas, A. Michaelides, E. C. H. Sykes, *Nat. Mater.* **2015**, DOI: 10.1038/nmat4323.
[14] G. Le Lay, *Nat. Nanotechnol.* **2015**, *10*, 202–203.
[15] Q. H. Wang, K. Kalantar-Zadeh, A. Kis, J. N. Coleman, M. S. Strano, *Nat. Nanotechnol.* **2012**, *7*, 699–712.
[16] V. Perebeinos, *Nat. Nanotechnol.* **2015**, *10*, 485–486.
[17] X. Zhang, J. Zhang, J. Zhao, B. Pan, M. Kong, J. Chen, Y. Xie, *J. Am. Chem. Soc.* **2012**, *134*, 11908–11911.
[18] J. Yuan, J. Lou, *Nat. Nanotechnol.* **2015**, *10*, 389–390.
[19] M. Guan, C. Xiao, J. Zhang, S. Fan, R. An, Q. Cheng, J. Xie, M. Zhou, B. Ye, Y. Xie, *J. Am. Chem. Soc.* **2013**, *135*, 10411–10417.
[20] F. Song, X. Hu, *Nat. Commun.* **2014**, *5*, 4477.
[21] F. Saleem, Z. Zhang, B. Xu, X. Xu, P. He, X. Wang, *J. Am. Chem. Soc.* **2013**, *135*, 18304–18307.

[22] J. N. Coleman, M. Lotya, A. O'Neill, S. D. Bergin, P. J. King, U. Khan, K. Young, A. Gaucher, S. De, R. J. Smith, I. V. Shvets, S. K. Arora, G. Stanton, H.-Y. Kim, K. Lee, G. T. Kim, G. S. Duesberg, T. Hallam, J. J. Boland, J. J. Wang, J. F. Donegan, J. C. Grunlan, G. Moriarty, A. Shmeliov, R. J. Nicholls, J. M. Perkins, E. M. Grieveson, K. Theuwissen, D. W. McComb, P. D. Nellist, V. Nicolosi, *Science* **2011**, *331*, 568 – 571.
[23] X. Huang, Z. Zeng, H. Zhang, *Chem. Soc. Rev.* **2013**, *42*, 1934 – 1946.
[24] K.-K. Liu, W. Zhang, Y.-H. Lee, Y.-C. Lin, M.-T. Chang, C.-Y. Su, C.-S. Chang, H. Li, Y. Shi, H. Zhang, C.-S. Lai, L.-J. Li, *Nano Lett.* **2012**, *12*, 1538 – 1544.
[25] Y. Xia, Y. Xiong, B. Lim, S. E. Skrabalak, *Angew. Chem. Int. Ed.* **2009**, *48*, 60 – 103; *Angew. Chem.* **2009**, *121*, 62 – 108.
[26] A. R. Tao, S. Habas, P. Yang, *Small* **2008**, *4*, 310 – 325.
[27] J. Gu, Y.-W. Zhang, F. Tao, *Chem. Soc. Rev.* **2012**, *41*, 8050 – 8065.
[28] D. Wang, Y. Li, *Adv. Mater.* **2011**, *23*, 1044 – 1060.
[29] M. Chen, B. Wu, J. Yang, N. Zheng, *Adv. Mater.* **2012**, *24*, 862 – 879.
[30] H. Duan, N. Yan, R. Yu, C.-R. Chang, G. Zhou, H.-S. Hu, H. Rong, Z. Niu, J. Mao, H. Asakura, T. Tanaka, P. J. Dyson, J. Li, Y. Li, *Nat. Commun.* **2014**, *5*, 3093.
[31] R. Jin, Y. Cao, C. A. Mirkin, K. L. Kelly, G. C. Schatz, J. G. Zheng, *Science* **2001**, *294*, 1901 – 1903.
[32] J. E. Millstone, S. J. Hurst, G. S. Métraux, J. I. Cutler, C. A. Mirkin, *Small* **2009**, *5*, 646 – 664.
[33] X. Zhang, Y. Xie, *Chem. Soc. Rev.* **2013**, *42*, 8187 – 8199.
[34] Y. Sun, H. Cheng, S. Gao, Q. Liu, Z. Sun, C. Xiao, C. Wu, S. Wei, Y. Xie, *J. Am. Chem. Soc.* **2012**, *134*, 20294 – 20297.
[35] Z. Lu, Z. Chang, W. Zhu, X. Sun, *Chem. Commun.* **2011**, *47*, 9651 – 9653.
[36] M. Cheng, M. Wen, S. Zhou, Q. Wu, B. Sun, *Inorg. Chem.* **2012**, *51*, 1495 – 1500.
[37] Z. Lu, M. Sun, T. Xu, Y. Li, W. Xu, Z. Chang, Y. Ding, X. Sun, L. Jiang, *Adv. Mater.* **2015**, *27*, 2361 – 2366.
[38] Z. Lu, W. Zhu, X. Yu, H. Zhang, Y. Li, X. Sun, X. Wang, H. Wang, J. Wang, J. Luo, X. Lei, L. Jiang, *Adv. Mater.* **2014**, *26*, 2683 – 2687.
[39] T. Fujita, P. Guan, K. McKenna, X. Lang, A. Hirata, L. Zhang, T. Tokunaga, S. Arai, Y. Yamamoto, N. Tanaka, Y. Ishikawa, N. Asao, Y. Yamamoto, J. Erlebacher, M. Chen, *Nat. Mater.* **2012**, *11*, 775 – 780.
[40] M. Gong, W. Zhou, M.-C. Tsai, J. Zhou, M. Guan, M.-C. Lin, B. Zhang, Y. Hu, D.-Y. Wang, J. Yang, S. J. Pennycook, B.-J. Hwang, H. Dai, *Nat. Commun.* **2014**, *5*, 4695.

Received: October 14, 2015
Published online: November 19, 2015

